ARTICLE OPEN

Check for updates

Controllable tunability of a Chern number within the electronic-nuclear spin system in diamond

Junghyun Lee [1,2,11], Keigo Arai[3,4,11], Huiliang Zhang[3,5], Mark J. H. Ku[3,5,6,7] and Ronald L. Walsworth [3,5,8,9,10 ✉]

Chern numbers characterize topological phases in a wide array of physical systems. However, the resilience of system topology to external perturbations makes it challenging experimentally to investigate transitions between different phases. In this study, we demonstrate the transitions of a Chern number from 0 to 3, synthesized in an electronic-nuclear spin system associated with the nitrogen-vacancy (NV) centre in diamond. The Chern number is characterized by the number of degeneracies enclosed in a control Hamiltonian parameter sphere. Topological transitions between different phases are realized by varying the radius and offset of the sphere such that the Chern number changes. We show that the measured topological phase diagram is consistent with numerical calculations and can also be mapped onto an interacting three-qubit system. The NV system may also allow access to even higher Chern numbers, which could be applied to exploring exotic topology or topological quantum information.

INTRODUCTION

Currently, extensive research is being conducted on the topologically invariant Chern number[1], which is defined as the integral of the Berry curvature of the system of interest[2–6], and on the application of its robust topological properties to quantum metrology[7], next-generation electronics[8], spintronics[9], and quantum computation[10–13]. Particularly, exploration of the Chern number at higher values and investigating the transitions between different Chern numbers are of significant interest[14–16]. For example, high Chern number phases in quantum anomalous Hall insulators are a candidate platform for next-generation low-power-consumption electronics, because the contact resistance between normal metal electrodes and chiral edge channels drops as the Chern number increases[17–19]. To characterize this scaling experimentally, it is necessary to vary the Chern number without changing the material properties.

The Berry curvature and Chern number are used to characterize the topological properties of the Hamiltonian parameter space for a quantum system of interest. In particular, the Berry curvature can be visualized as the field lines of a pseudo magnetic monopole associated with a quantum system under certain conditions[20], while the Chern number represents the number of these monopoles within a closed surface in the system's parameter space. In a two-dimensional lattice system, the source of Berry flux (and hence curvature) in momentum space is a point where two bands touch, known as the degeneracy or Dirac point[21] of the Brillouin zone; whereas in a two-level system, the degeneracy point coincides with the resonance condition (on-resonance point in parameter space) at which the length of the associated Bloch vector becomes zero.

Despite an advanced theoretical foundation, Chern numbers greater than one have only recently been studied experimentally in condensed matter systems, e.g., in multilayer-graphene boron-nitride interfaces with field-tunable superlattice flat bands[14,22];

and in undoped multilayers of a topological insulator under alternating magnetic fields[8,23]. Moreover, although controllability of the Chern number will add significant value to the above-mentioned practical applications, it is even more challenging to transit across topological phases. Two major challenges hinder such experimental investigation: namely, continuous tuning of the properties in materials; and direct detection of the topological invariant of multi-fold degenerate points in condensed matter systems.

An alternative approach to studying Chern numbers experimentally involves the use of two-level systems[24–27] in various qubit platforms, including superconducting qubits[28–30], ultracold atoms[31–34], and nitrogen vacancy (NV) centres in diamond[35,36]. These platforms have many, well-controlled experimental degrees of freedom that can be employed as powerful quantum simulators for complex and dynamic Hamiltonian models in condensed matter systems, which are otherwise difficult to access. Notably, researchers have used a single NV centre to explore 2D synthetic quantum Hall physics[37], a topological phase transition of a quantum wire[38], and a synthetic monopole source in the Kalb-Ramond field[39].

According to Gritsev et al.[40], the Chern number can be measured as an integral of the deviation in the qubit Bloch vector from the hemispherical trajectory of a time-varying Larmor vector, owing to a nonadiabatic response (Fig. 1a). Here, we assume that the qubit system can be described by the generic Hamiltonian $\hat{H}(t) = \hat{H}_S + \hat{H}_C(t)$, where $\hat{H}_S$ is the static internal Hamiltonian that defines the degeneracy points, and $\hat{H}_C(t)$ is the time-dependent control Hamiltonian. The control Hamiltonian adopts the form $\hat{H}_C(t) = -\hbar \mathbf{H}(t) \cdot \boldsymbol{\sigma}/2$, where $\hbar$ is the reduced Planck's constant, $\mathbf{H}(t)$ is the time-varying Larmor vector in a three-dimensional Hamiltonian parameter space labelled as (H_x, H_y, H_z), and $\boldsymbol{\sigma} = (\sigma^x, \sigma^y, \sigma^z)$ are the Pauli matrices. The Larmor vector is chosen to sweep a hemispherical trajectory from

[1]Department of Physics, Massachusetts Institute of Technology, Cambridge, MA 02139, USA. [2]Center for Quantum Information, Korea Institute of Science and Technology, Seoul 02792, Republic of Korea. [3]Harvard-Smithsonian Center for Astrophysics, Cambridge, MA 02138, USA. [4]Department of Electrical and Electronic Engineering, Tokyo Institute of Technology, Tokyo 152-8552, Japan. [5]Department of Physics, Harvard University, Cambridge, MA 02138, USA. [6]Department of Physics and Astronomy, University of Delaware, Newark, DE 19716, USA. [7]Department of Materials Science and Engineering, University of Delaware, Newark, DE 19716, USA. [8]Quantum Technology Center, University of Maryland, College Park, MD 20742, USA. [9]Department of Electrical and Computer Engineering, University of Maryland, College Park, MD 20742, USA. [10]Department of Physics, University of Maryland, College Park, MD 20742, USA. [11]These authors contributed equally: Junghyun Lee, Keigo Arai. ✉email: walsworth@umd.edu
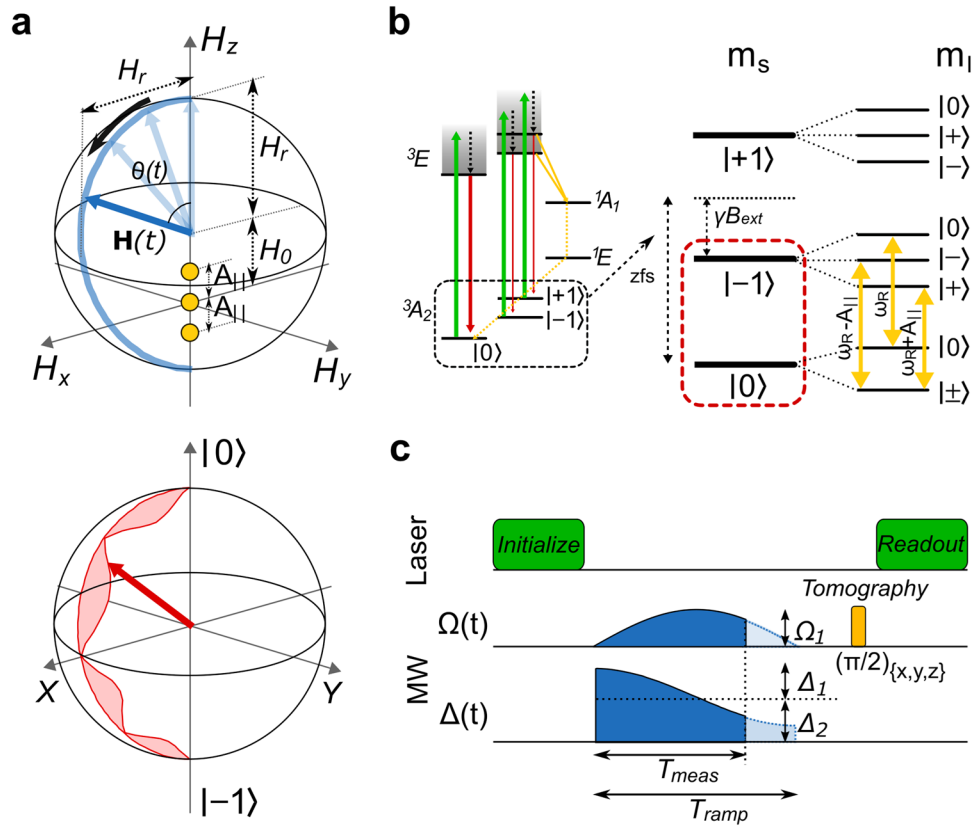
npj

Fig. 1 Schematic of Chern number measurement with an NV centre in diamond. a Upper: Trajectory of the Larmor vector $\mathbf{H}(t)$ is represented by a thick blue arrow in the spherical control Hamiltonian parameter space (H_x, H_y, H_z). The solid black arrow indicates the direction of the sweep of the Larmor vector. The yellow circles represent the degeneracy points of the system Hamiltonian. Lower: Time evolution of the NV electronic spin Bloch vector $\boldsymbol{\sigma}(t)$ is represented by the red arrow on the Bloch sphere. The Bloch vector path deviates from the Larmor vector path due to a nonadiabatic response. The red filled area indicates the amount of deviation, a summation of which over the path is related to the Chern number. **b** NV centre energy level diagram. The NV ground states consist of $|0\rangle$, $|\pm 1\rangle$ electronic spin sublevels, which are further split by hyperfine interactions with the host ^{14}N nuclear spin. Three hyperfine transitions between $|0\rangle$ and $|-1\rangle$ electronic spin sublevels (yellow double-arrows) define three degeneracy points in the rotating frame with angular speeds of $\omega_R - A_\parallel$, ω_R, $\omega_R + A_\parallel$, where $A_\parallel$ is the parallel component of the hyperfine tensor. **c** Experimental pulse sequence. An optical initialization pulse polarizes the electronic spin into $|0\rangle$. Then, a microwave pulse with time-varying Rabi frequency $\Omega(t) = \Omega_1 \sin\theta(t)$ and time-varying detuning $\Delta(t) = \Delta_1 \cos\theta(t) + \Delta_2$ under a constraint of $\Omega_1 = \Delta_1$ realizes the Larmor vector trajectory. This pulse is terminated at $t = T_{meas}$. The Larmor vector trajectory is completed within a time of T_{ramp}. The combination of a microwave tomography pulse and a laser readout pulse allows the measurement of all the Bloch vector components.

the north pole to the south pole with a radius H_r and by introduction of an offset H_0 along the z-axis from the origin:

$$\mathbf{H}(t) = (H_r \sin\theta(t)\cos\phi(t), H_r \sin\theta(t)\sin\phi(t), H_r \cos\theta(t) + H_0), \quad (1)$$

where θ is the time-varying polar angle and ϕ is the azimuthal angle fixed at 0, without loss of generality. When the Larmor vector traverses this trajectory at a finite speed, the qubit's Bloch vector $\langle\boldsymbol{\sigma}\rangle$ follows the Larmor vector $\mathbf{H}(t)$, but with a small deviation along the ϕ direction at each polar angle location owing to a nonadiabatic response[2–4,41]. For a first-order approximation, this deviation is related to the ϕ component of the Berry curvature F_ϕ through the following linear relation:

$$F_\phi(\theta) = \frac{H_r \sin\theta\langle\sigma^y\rangle}{2v_\theta}, \quad (2)$$

where $\langle\sigma^y\rangle$ is the expectation value of the y component of the Bloch vector and $v_\theta \equiv d\theta/dt$ denotes the angular speed about its polar axis. Integration of this Berry curvature over the polar angle of the trajectory yields the Chern number as follows:

$$C = \int_0^\pi F_\phi(\theta)d\theta. \quad (3)$$

Here, the Chern number depends on the number of degeneracy points of the static internal Hamiltonian enclosed in a control Hamiltonian sphere drawn by the Larmor vector. Every degeneracy point can be regarded as a synthetic magnetic monopole. These monopoles produce radial synthetic magnetic fields that exert a torque on the Bloch vector.

In this work, we apply the above protocol to experimentally observe the transition of the Chern number from 0 to 3, using three degeneracy points associated with the ground-state spin energy levels of a single NV centre in diamond (Fig. 1b). In this electronic-nuclear spin hybrid system, parameter space degeneracy points correspond to on-resonance conditions between the hyperfine-split energy levels. The NV electronic spin ground-state has three sublevels $|-1\rangle$, $|0\rangle$, and $|+1\rangle$, out of which only $|-1\rangle$ and $|0\rangle$ are used here as a two-level system, represented by $\boldsymbol{\sigma}$ in the following measurements. The NV host nuclear spin ^{14}N, with a spin quantum number of $I = 1$, induces a hyperfine coupling. The associated internal Hamiltonian takes the form $\hat{H}_0 = (\hbar/2)A_\parallel \sigma^z I^z$, where $A_\parallel/2\pi = 2.2$ MHz is the coupling strength of the longitudinal component of the hyperfine interaction and I_z denotes the z component of the nuclear spin. This electronic-nuclear spin system contains three degeneracy points, allowing us to access
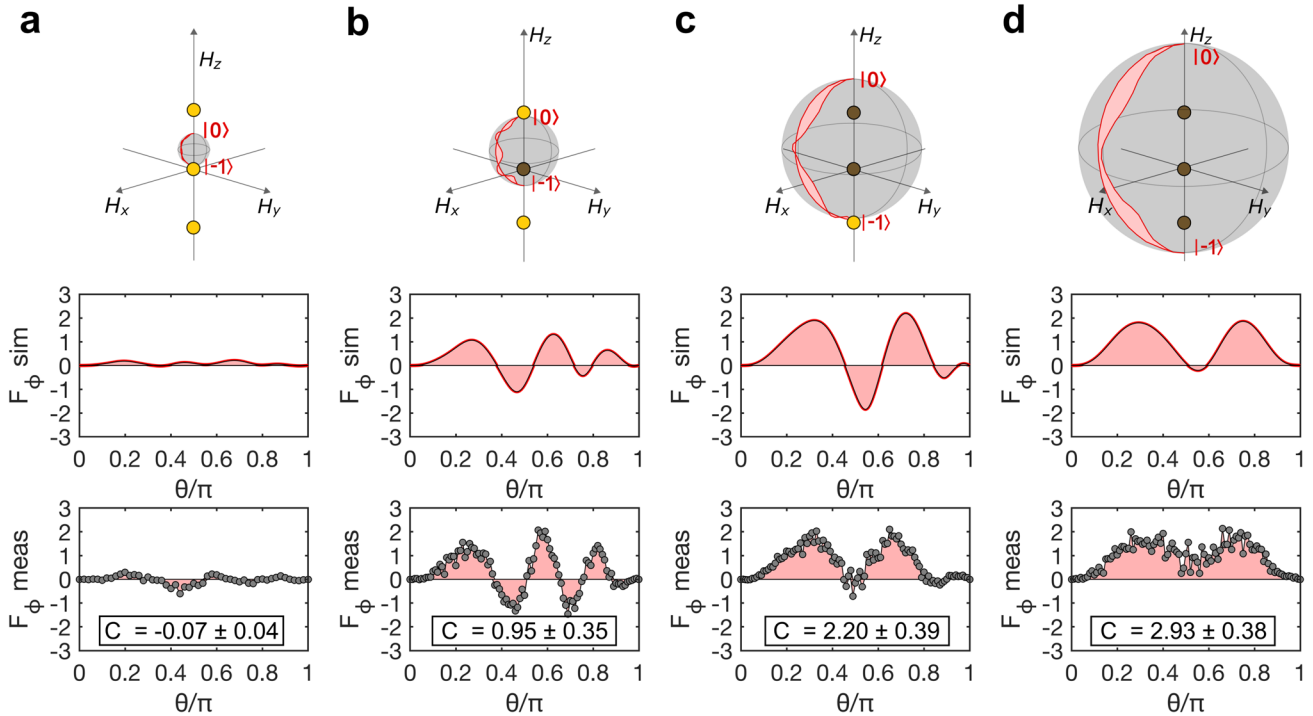
Fig. 2 Observation of Chern numbers from 0 to 3. The number of degeneracy points included in the control Hamiltonian parameter sphere is incremented one by one by enlarging the normalized sphere radius $H_r/A_\parallel$ under a fixed offset of $H_0/A_\parallel = 0.23$. **a** Case with no degeneracy points within the sphere. Expected Chern number is $C = 0$. Top sphere is an illustration of the Bloch vector trajectory (red line) overlaid with the degeneracy points (yellow circles) and the control Hamiltonian parameter sphere (grey). Numerically simulated Berry curvature $F_\phi^{sim}(\theta)$ (red line) presented in the middle. Measured Berry curvature $F_\phi^{meas}(\theta)$ (grey points and red shaded area) at the bottom. Integrating the Berry curvature over θ gives a Chern number of $C = -0.07 \pm 0.04$. **b–d** Cases with one, two, and three degeneracy points, respectively: yellow (black) circles lie outside (inside) the control Hamiltonian parameter spheres (grey). Expected Chern numbers are $C = 1, 2, 3$, while the measured Chern numbers are $C = 0.95 \pm 0.35, 2.20 \pm 0.39, 2.93 \pm 0.38$.

the topological phases with a Chern number greater than 1. The time-dependent Larmor vector in Eq. (1) is realized through application of spin-control microwave fields that exhibit a time-varying Rabi frequency $\Omega(t) = \Omega_1 \sin\theta(t)$ and detuning of $\Delta(t) = \Delta_1 \cos\theta(t) + \Delta_2$, both described in units of Hz. Under this experimental configuration, the Larmor vector can be written as the time-dependent Hamiltonian:

$$\mathbf{H}(t) = (\Omega_1 \sin\theta(t), 0, \Delta_1 \cos\theta(t) + \Delta_2). \quad (4)$$

Figure 1c illustrates the experimental sequence for measuring the Berry curvature at a specific polar angle. The hemispherical trajectory of the Larmor vector starts from the north pole $\theta = 0$ at $t = 0$ and ramps along the $H_y = 0$ meridian with a constant angular velocity until it reaches the south pole $\theta = \pi$ at $t = T_{ramp}$, that is, $\theta(t) = \pi t (T_{ramp})^{-1}$. Throughout this study, the direction of the trajectory is fixed along the north-to-south direction with respect to the points of ground-state degeneracy. A snapshot of the NV electronic spin Bloch vector component $\langle\sigma^y\rangle$ at various polar angle locations is obtained by terminating the sweep at time $t = T_{meas}$.

As a measure of the degree of adiabaticity, an adiabaticity parameter[27] is introduced as follows:

$$a \equiv \frac{\Omega_1 T_{ramp}}{2\pi}. \quad (5)$$

This parameter represents the fractional change in the Larmor vector. Recalling the extra second-order term $O(v^2)$ in the Berry curvature formula (Supplementary Eq. 3), a characterizes the accuracy of the measured Chern number. In the nonadiabatic limit ($a \ll 1$), the first-order approximation of the Berry curvature in Eq. (2) breaks down. Subsequently, the effects of higher-order terms

contaminate the signal in our measurements. Conversely, in the adiabatic limit ($a \gg 1$), the NV electronic spin remains in the instantaneous ground state; and the spin Bloch vector is approximately parallel to the direction of the control field, following the meridian. However, the deviation signal $\langle\sigma^y\rangle$ becomes smaller and eventually lies buried in measurement noise. For the three-level NV system, the appropriate range reflecting an optimum signal-to-noise ratio is found to be $2 \leq a \leq 10$ (see Supplementary Fig. 1). The adiabaticity parameter is set to $a = 2$ for the remainder of the work.

RESULTS

Chern number transition from 0 to 3

As a benchmark experiment, we first characterize a case with the expected Chern number of $C = 0$ (Fig. 2a). This case is realized by choosing a small control Hamiltonian sphere with a normalized radius of $H_r/A_\parallel = 0.2$ and a normalized detuning of $H_0/A_\parallel = 0.23$, which does not contain any of the three degeneracy points. Although these degeneracy points are expected to make the Berry-curvature zero for any θ, numerical simulations based on a time-dependent Schrödinger equation (see Methods) predict a deviation from zero. This deviation can be attributed to the nonadiabatic effect, which limits the accuracy of this quasi-static Chern number measurement approach. The measured Berry curvature is consistent with the simulation results, including the nonadiabatic effect. The resulting Chern number, obtained by integrating the measured Berry curvature over theta, converges to $C = -0.07 \pm 0.04$. Measurement error is evaluated from the photon-shot noise (1σ).
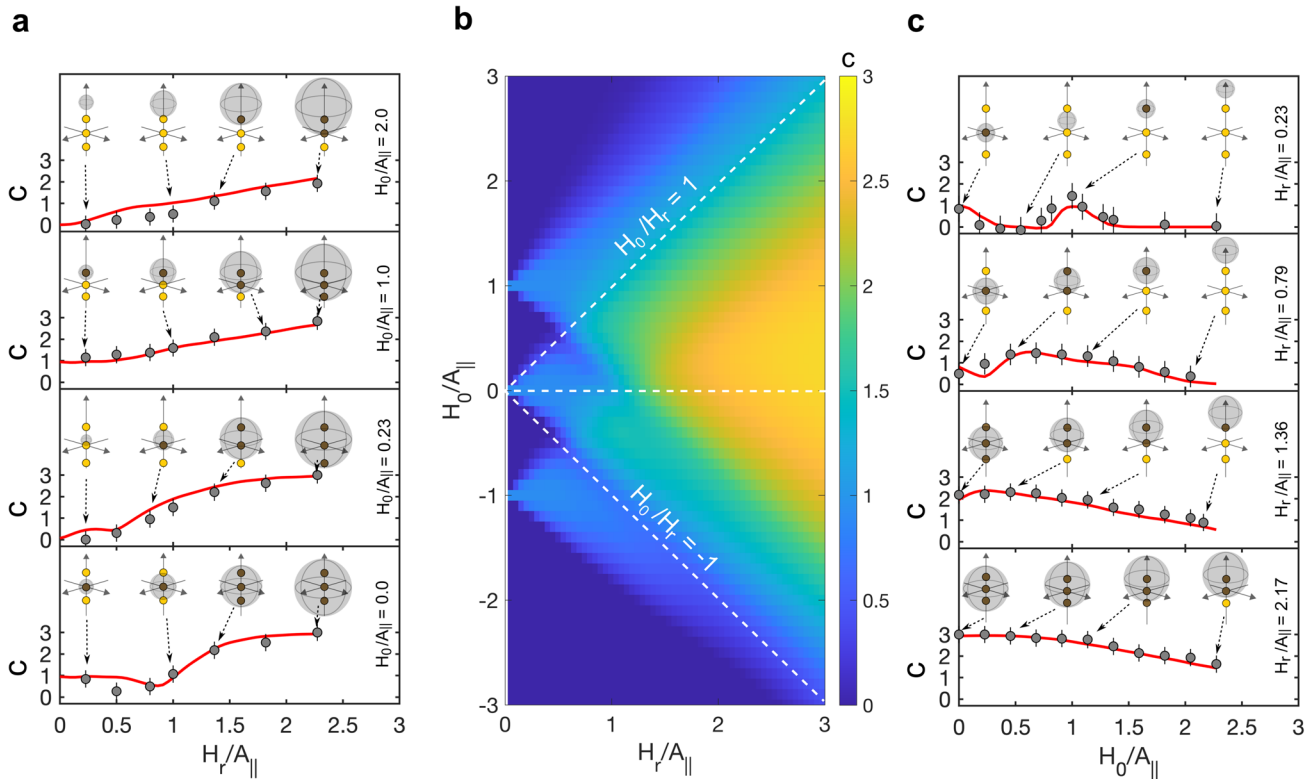
Fig. 3 Two-dimensional topological phase diagram and phase transitions along the vertical and horizontal directions. a Measured (grey circles) and simulated (red solid line) Chern number values along the normalized radius $H_r/A_\parallel$ direction under a fixed normalized offset of $H_0/A_\parallel = 2.00, 1.00, 0.23, 0.00$. Control Hamiltonian parameter spheres (grey) and degeneracy points (yellow and black) are shown for each case. **b** Numerically simulated topological phase map. White dashed lines along $H_0/H_r = \pm1$ are presented as a guide for eye. Asymmetry in the pattern with respect to $H_0/A_\parallel = 0$ is attributed to the time-reversal symmetry breaking of the measurement protocol. **c** Measured (grey circles) and simulated (red solid line) Chern number values along the normalized offset $H_0/A_\parallel$ for a fixed normalized radius of $H_r/A_\parallel = 0.23, 0.79, 1.36, 2.17$. Control Hamiltonian parameter spheres (grey) and degeneracy points (yellow and black) are shown for each case.

To observe higher Chern numbers, we next examine cases with one, two, and three enclosed degeneracy points by increasing the radius up to $H_r/A_\parallel = 2.25$ (Fig. 2b–d). Numerical simulations predict a larger deviation in the path of the Bloch vector with an increase in the number of enclosed degeneracy points, indicating more pronounced behaviour for the Berry curvature. The measured Berry curvatures for each case agree well with the numerically simulated values. The Chern numbers are determined to be $C = 0.95 \pm 0.35$, 2.20 ± 0.39, and 2.93 ± 0.38. Thus, our results demonstrate that the NV electronic-nuclear spin system can be used as a platform for synthesizing up to three Chern numbers.

Three monopole 2D phase transition diagram

The NV system can further explore the transition between the observed Chern numbers. Figure 3a presents measurements of the topological phase transition along the normalized radius axis ($H_r/A_\parallel \in \{0.25, 2.25\}$) for various normalized offset conditions: $H_0/A_\parallel = 2.0, 1.0, 0.23, 0.0$. In all cases, we observe a mild phase transition, which can be attributed to the finite NV electronic spin coherence (T_2^*) time and the limited adiabaticity parameter a. Additionally, the observed consistency between experimentally measured and numerically simulated Chern numbers reflects this nonadiabatic effect within one standard deviation of the measurement error, except for $H_r/A_\parallel \leq 1$. The disagreement within this small-radius region may be due to imperfect system calibration at low Rabi frequencies (see Methods). One notable effect is found in the case of $H_0/A_\parallel = 0.0$, where the number of

enclosed degeneracy points is expected to jump from one to three at $H_r/A_\parallel = 1$. However, in the measurements, a sudden depletion of C is observed below 1, and the transition is found to occur above 1. This shift in the transition point can be attributed to the nonadiabatic response of a qubit when the Larmor vector coincides with the position of the degeneracy points on the z-axis. Figure 3c presents the observed transition curves across the normalized offset ($H_0/A_\parallel \in \{0.00, 2.25\}$) for various values of the normalized radius of $H_r/A_\parallel = 0.23, 0.79, 1.36, 2.17$, indicating the diversity of the phase transition pattern.

A systematic assessment of the measurement results can be obtained by mapping the Chern number phase diagram onto a two-dimensional parameter space of $H_0/A_\parallel$ and $H_r/A_\parallel$ (Fig. 3b). It is found that the Chern number distribution is not mirror-reflected with respect to the $H_0/A_\parallel = 0$ line. This asymmetry occurs due to the time-reversal symmetry breaking of the system[42] when $C \neq 0$, which is caused by the sweeping of the Larmor vector from positive to negative detuning during the measurement, creating a directional dependence of the Lorentzian force-like response of the qubit; thereby, breaking the Chern number transition symmetry (see Supplementary Discussion).

DISCUSSION

We next discuss the connection (i.e., mapping) between the NV system in our experiments and an interacting three-qubit system to reveal the implications of our observed two-dimensional topological phase diagram[29]. The topological phase diagram presented in this study is constructed by varying the radius and
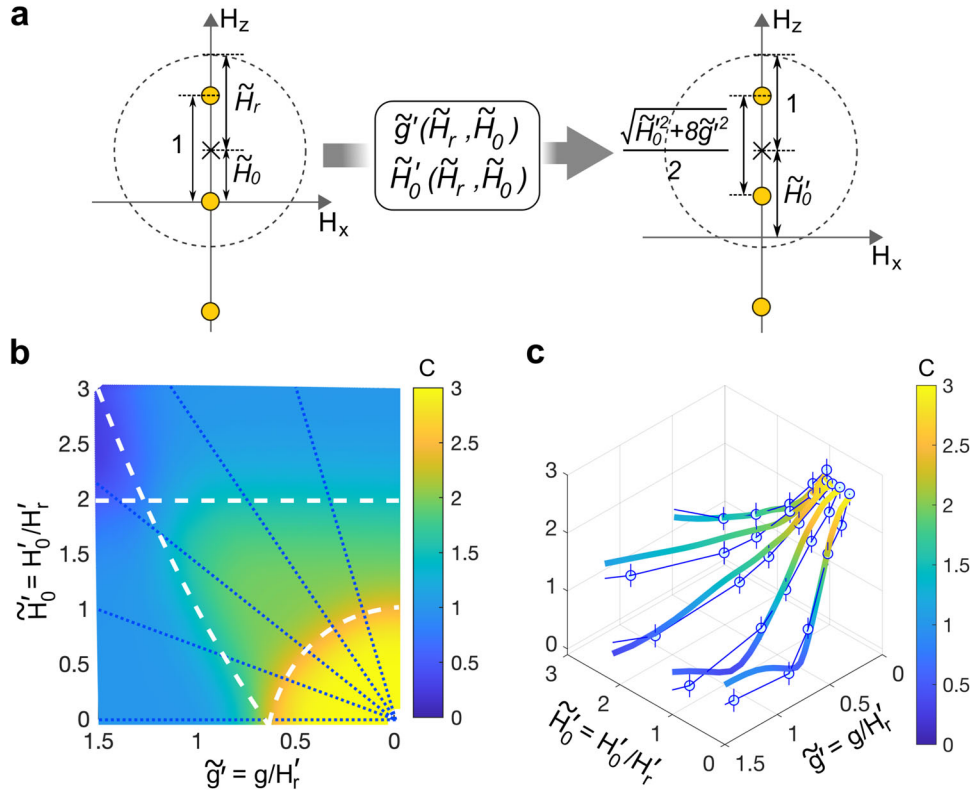
Fig. 4 Tunable topological invariant with three monopoles. a Topological equivalence of the Chern number measurement using the electronic-nuclear spin system of the NV centre and three interacting qubits. (left) Degeneracy points of the NV electronic-nuclear spin system (yellow circles) relative to a 2D slice of the control Hamiltonian parameter sphere (dashed line). The inter-degeneracy spacing $A_{\parallel}$ is constant, whereas the radius H_r and offset H_0 are variable. (right) Degeneracy points of the equispaced interacting three-qubit system. The inter-qubit coupling strength g and the radius H'_r are variable, while the offset H'_0 is fixed. **b** Simulated Chern number phase diagram for the interacting three-qubit Hamiltonian. White dashed lines indicate the transition boundaries; blue dotted lines denote the radial cross-sections presented in (**c**). **c** Projected three-monopole Chern number measurements (blue open circle); and cross-sectional transition of a simulated three-qubit phase diagram (parula colourmap). Sweep parameters are normalized for attaining a unitless topology (three-monopole system normalized by $A_{\parallel}$ and three-qubit system normalized by H'_r). Each radial projection corresponds to a fixed $\tilde{H}_0 = 0$, 0.23, 0.45, 0.68 and 0.91.

offset of the control Hamiltonian sphere with respect to the three degeneracy points. As shown in Fig. 4a, varying the radius under fixed inter-degeneracy spacings is topologically similar to varying the inter-degeneracy spacing under a fixed radius. The former is implemented in this work using the NV centre, which can be regarded as a single qubit that has an Ising interaction with an additional spin with a large quantum number. The latter can be realized by varying the coupling strength g in an interacting symmetric 1D chain three qubit system using the following Hamiltonian:

$$\hat{H}_{3q} = -\frac{\hbar}{2}\big(\mathbf{H_1}\cdot\boldsymbol{\sigma_1}+\mathbf{H_2}\cdot\boldsymbol{\sigma_2}+\mathbf{H_3}\cdot\boldsymbol{\sigma_3}+H'_0\sigma_1^z+\tfrac{1}{2}H'_0\sigma_2^z$$
$$-g(\sigma_1^x\sigma_2^x+\sigma_1^y\sigma_2^y)-g(\sigma_2^x\sigma_3^x+\sigma_2^y\sigma_3^y)\big). \quad (6)$$

The topological phases measured in these two systems can be mathematically connected via projection functions:

$$\tilde{g}'(\tilde{H}_r,\tilde{H}_0) = \frac{1}{2\tilde{H}_r}\sqrt{1-(1-|1-2\tilde{H}_0|)^2},$$
$$\tilde{H}'_0(\tilde{H}_r,\tilde{H}_0) = \frac{1}{\tilde{H}_r}(1-|1-2\tilde{H}_0|), \quad (7)$$

where $\tilde{g}' = g/H_r$, $\tilde{H}'_0 = H_0/H_r$, $\tilde{H}_r = H_r/A_{\parallel}$, and $\tilde{H}_0 = H_0/A_{\parallel}$.

As shown in Fig. 4b, we numerically calculate the topological phase diagram of the interacting three-qubit system. For a large H_r, where the Rabi frequency becomes significantly larger than $A_{\parallel}$, the normalized coupling strength $\tilde{g}'$ approaches 0, where the three qubits distinctively contribute to the total Chern number such that $C = 3$. Owing to the inverse relation, when $\tilde{H}_r$

approaches 0, both $\tilde{g}'$ and $\tilde{H}'_0$ become large, where $C = 0$ in the phase diagram. The Chern number behaviour for these limiting cases remains similar to that of the coupled two-qubit Hamiltonian[25]. Meanwhile, a more complex phase structure can be found by analytically calculating the positions of the ground state degeneracy points with respect to the sweep parameter sphere manifold. The white dashed boundaries clarify four distinctive regions where the Chern number in each region corresponds to the number of monopoles enclosed by the surface. Along the $\tilde{H}'_0$ axis, one monopole exits the surface at $\tilde{H}'_0 = 1$ ($C = 3$ to $C = 2$) and secondly at $\tilde{H}'_0 = 2$ ($C = 2$ to $C = 1$). Next, along the $\tilde{g}'$ axis, the two monopoles escape the surface at $\tilde{g}' = 1/\sqrt{2}$, inducing the Chern number transition from $C = 3$ to $C = 1$.

Finally, we project the NV three-monopole topological phase measurements onto the interacting three-qubit system using Eq. (7) and then compare with the three-qubit Chern number simulation results (Fig. 4c). For a fixed $\tilde{H}_0$, H_r is swept from 0.22 to 2.2 by varying the Rabi frequency on the NV spin. The orthogonal parameter axes, $\tilde{H}_0$ and $\tilde{H}_r$, are nonlinearly transformed into $\tilde{H}'_0$ and $\tilde{g}'$, which gives topological phase transition curves in radial cross-sections for $\tilde{H}_0 = 0$, 0.23, 0.45, 0.68, and 0.91. The three-monopole Chern number transition projection, evaluated using Eq. (8), and the simulated Chern number transition cross section of the interacting three-qubit system are consistent with each other (blue dotted line in Fig. 4b).

The coupled multiqubit Hamiltonian carries multiple degenerate ground states, which leads to the realization of a high Chern number. Here, the interaction strength, g, between qubits

determines the position of the monopoles on the parameter space z-axis (see Supplementary Methods). In principle, investigating the topology of an N-interacting qubit system could simulate the topology of non-interacting $2N$ band models. For example, two interacting qubit systems, simulating the topology of the ground band of a four-band electronic model, together with an interacting three-qubit system could help to probe the topological structure of the half-filled eight-band model[29].

Our scheme clearly shows that a high Chern number can be deterministically simulated using a single-qubit-based multi-monopole system, in addition to tuning the level of its transition depending on the range of $H_0/A_\parallel$ and $H_r/A_\parallel$ variations. In particular, the electron-nuclear spin-coupled NV system in diamond can be a versatile tool for studying a high-dimensional topology; e.g., further scaling up to a higher topologically-invariant number can be straightforwardly performed, in principle, by utilizing the intrinsic ^{13}C nuclear spins near the NV electronic spin qubit, with hyperfine coupling strengths varying from a few tens of kHz to almost ~100 MHz[43]. For a higher-number symmetric monopole system, one can engineer the Chern number transition with an increment of 1, or an even number transition, $C = 0, 2, 4 \cdots$, or an odd number transition $C = 1, 3, 5 \cdots$, by adjusting the detuning $H_0/A_\parallel$.

In this work, we simulate a high topologically-invariant number (the Chern number, C) using the experimentally accessible system of a single NV electronic spin qubit that is hyperfine coupled with the host ^{14}N nuclear spin. We also demonstrate the robust tunability of the measured Chern number up to $C = 3$ by harnessing the control parameters of the qubit. A systematic design of the Hamiltonian parameter sphere reveals the detailed topological structures over three synthetic monopoles, as well as intriguing Chern number physics associated with the adiabaticity of the system's evolution over time. The generality of this method can be expanded to various qubit platforms to investigate the topology of higher dimensions, such as N-interacting qubit systems, which can simulate the topology of non-interacting $2N$ band models in condensed-matter physics. Furthermore, the tunability of the topological invariant of a qubit system can be directly applied to explore more exotic topology, which could be applied to the field of topological quantum information science.

METHODS

NV spin system with three degeneracies
The NV centre ground-state has an electronic spin with quantum number $S = 1$ and sublevels $|0\rangle$ and $|\pm1\rangle$. Throughout this work, we use only sublevels $|0\rangle$ and $|-1\rangle$ as a two-level system, by Zeeman splitting the $|\pm1\rangle$ states using a static external bias magnetic field. The NV electronic spin experiences a hyperfine interaction with the host nuclear spin ^{14}N, with spin quantum number $I = 1$. The longitudinal component of the hyperfine interaction, with coupling strength $A_\parallel/2\pi = 2.2$ MHz, further splits the $|-1\rangle$ sublevel into three hyperfine levels. The internal NV Hamiltonian assumes the form $H_0 = (\hbar/2)A_\parallel\sigma^z I^z$. Consequently, this electronic-nuclear spin system contains three degeneracy points, allowing us to simulate topological phases with a Chern number greater than 1. Additionally, the transition between different Chern numbers can be realized by introducing a common offset to these degeneracy points. The topology realized in this study corresponds to an eight-band noninteracting triangular lattice model.

Experimental setup
Measurements are performed using a home-built NV-diamond confocal microscope. An acousto-optic modulator (Isomet Corporation) enables time gating of a 400 mW, 532 nm diode-pumped solid-state laser (Changchun New Industries). The laser beam is coupled to a single-mode fibre, and subsequently, delivered to an oil-immersion objective (×100, 1.3 NA, Nikon CFI Plan Fluor), and focused onto a diamond sample. The diamond sample is fixed on a three-axis motorized stage (Micos GmbH) for precise position control. NV red fluorescence (FL) is collected using the same objective and then passed through a dichroic filter (Semrock LP02–633RS-25). A pinhole (diameter 75 μm) is used with an $f = 150$ mm telescope to spatially filter the FL signal, which is detected using a silicon avalanche photodetector (Perkin Elmer SPCM-ARQH-12). A signal generator (SG, Agilent E4428C) provides the carrier microwave signal. The phase and amplitude of the carrier signal is modulated with a 1 G s^{-1} rate arbitrary waveform generator (AWG, Tektronix AWG 5014 C) and an IQ mixer (Marki IQ 1545 LMP). The microwave sideband signal is amplified (Mini-circuits ZHL-16W-43-S+) and passed through a gold coplanar waveguide, fabricated on a quartz coverslip using photolithography that is mounted directly on the diamond sample to control the NV spin qubit. The diamond sample is CVD-grown, ^{12}C isotopically purified to 99.99%, with dimensions of 2 mm × 2 mm × 0.5 mm. The diamond is annealed at 800 °C for 8 h and then at 1000 °C for 10 h to mobilize vacancies in the diamond and, combined with existing nitrogen defects from the CVD process, to create the NV centre used in the experiment. During the measurement, the external magnetic field is aligned with the NV crystalline axis at a field strength of ~100 G. The measured NV spin resonance lifetimes are $T_1 \approx 3$ ms, Hahn-Echo $T_2 \approx 400$ μs, and $T_2^* \approx 40$ μs.

Quantum state tomography
To create a hemispherical trajectory of the Larmor vector and hence the NV electronic spin Bloch vector to follow, a sine-envelope-chirped microwave signal is used, with sweeping of both the detuning and Rabi frequency. To match the relative phase of the chirped signal, a tomography pulse is applied directly after the control pulse at a specific time T_{meas}. The $\langle\sigma^y\rangle$ rotation tomography pulse's relative phase is set with respect to the end phase of the chirped control signal. The tomography pulse Rabi frequency is set to 10 MHz. During calibration of the tomography pulse, the observed dynamic phase noise contribution is highly suppressed. The final NV electronic spin state is read out by optical illumination at 532 nm and measurement of the NV fluorescence (FL) in the 640–800 nm band over an observation time of 400 ns. A change in NV FL intensity occurs due to a non-radiative decay pathway via metastable singlet states (Fig. 1b). Measurements are repeated ~10^6 times to establish good statistics, given finite optical collection efficiency of the apparatus. Because the NV spin qubit system has two isolated spin levels in the presence of an external bias magnetic field (~100 G), leakage to other states can be neglected, which gives a fidelity advantage for using an NV centre for quantum simulations.

Adiabaticity parameter determination
We determine an optimized condition for the adiabaticity parameter a, where the NV electronic spin qubit response is quasi-adiabatic. This condition is fulfilled when (i) the qubit adiabatically follows the Larmor vector trajectory; and also (ii) the observable NV electronic spin Bloch vector component $\langle\sigma^y\rangle$, which is the Lorentzian deviation from the Larmor vector trajectory, has a sufficiently large signal-to-noise ratio to be detected. Using dynamic-state preparation as a benchmark of the adiabaticity parameter calibration[25], we first detect the Landau–Zener transition (Supplementary Fig. 3) by measuring $\langle\sigma^z\rangle$, the hemispherical manipulation of the NV spin qubit, and confirm that the transition probability depends on both the Rabi frequency Ω and T_{ramp} as expected. The Landau–Zener $\langle\sigma_z\rangle$ measurements, obtained by varying a, show that our system's quasi-adiabatic boundary is approximately with the $2 \leq a \leq 10$ range.

Numerical simulations

All numerical simulations of NV spin evolution in this work are performed by computing the time-ordered time evolution operator at each time step:

$$U(t_\mathrm{i}, t_\mathrm{f}) = \hat{\mathrm{T}}\left\{\exp\left(-i\int_{t_\mathrm{i}}^{t_\mathrm{f}} H(t)\mathrm{d}t\right)\right\} = \prod_{j=1}^{N}\exp\left(-i\Delta t H(t_j)\right) \qquad (8)$$

where t_i and t_f denote the initial and final time, respectively; $\hat{\mathrm{T}}$ is the time-ordering operator; Δt is the time step size of the simulation; $N = (t_\mathrm{f} - t_\mathrm{i})/\Delta t$ is the number of time steps; and $\hat{H}(t)$ is the time-dependent Hamiltonian. In the simulation, a step size of $\Delta t = 1$ ns is used, which is sufficiently small in the rotating frame. The algorithm is implemented using MATLAB® software.

DATA AVAILABILITY

The data supporting the findings of this study are available from the corresponding author upon reasonable request.

CODE AVAILABILITY

The codes and data used in this study are available from the corresponding author upon reasonable request.

REFERENCES

1. Chern, S.-S. Characteristic classes of Hermitian manifolds. *Ann. Math.* **47**, 85–121 (1946).
2. Berry, M. V. Quantal phase factors accompanying adiabatic changes. *Proc. R. Soc. Lond. A: Math. Phys. Sci.* **392**, 45–57 (1984).
3. Hannay, J. H. Angle variable holonomy in adiabatic excursion of an integrable Hamiltonian. *J. Phys. A: Math. Gen.* **18**, 221–230 (1985).
4. Suter, D., Mueller, K. T. & Pines, A. Study of the Aharonov-Anandan quantum phase by NMR interferometry. *Phys. Rev. Lett.* **60**, 1218–1220 (1988).
5. De Chiara, G. & Palma, G. M. Berry phase for a spin 1/2 particle in a classical fluctuating field. *Phys. Rev. Lett.* **91**, 090404 (2003).
6. Filipp, S. et al. Experimental demonstration of the stability of Berry's phase for a spin-1/2 particle. *Phys. Rev. Lett.* **102**, 030404 (2009).
7. Arai, K. et al. Geometric phase magnetometry using a solid-state spin. *Nat. Commun.* **9**, 4996 (2018).
8. Zhao, Y. F. et al. Tuning the Chern number in quantum anomalous Hall insulators. *Nature* **588**, 419–423 (2020).
9. Nagaosa, N. & Tokura, Y. Topological properties and dynamics of magnetic skyrmions. *Nat. Nanotechnol.* **8**, 899–911 (2013).
10. Hasan, M. Z. & Kane, C. L. Colloquium: topological insulators. *Rev. Mod. Phys.* **82**, 3045–3067 (2010).
11. Zanardi, P. & Rasetti, M. Holonomic quantum computation. *Phys. Lett. A* **264**, 94–99 (1999).
12. Zu, C. et al. Experimental realization of universal geometric quantum gates with solid-state spins. *Nature* **514**, 72–75 (2014).
13. Leibfried, D. et al. Experimental demonstration of a robust, high-fidelity geometric two ion-qubit phase gate. *Nature* **422**, 412–415 (2003).
14. Zhang, Y.-H., Mao, D., Cao, Y., Jarillo-Herrero, P. & Senthil, T. Nearly flat Chern bands in moiré superlattices. *Phys. Rev. B* **99**, 075127 (2019).
15. Fu, L., Kane, C. L. & Mele, E. J. Topological insulators in three dimensions. *Phys. Rev. Lett.* **98**, 106803 (2007).
16. Hatsugai, Y. Chern number and edge states in the integer quantum Hall effect. *Phys. Rev. Lett.* **71**, 3697–3700 (1993).
17. Chang, C.-Z. et al. Zero-field dissipationless chiral edge transport and the nature of dissipation in the quantum anomalous Hall state. *Phys. Rev. Lett.* **115**, 057206 (2015).
18. Wang, J., Lian, B., Zhang, H., Xu, Y. & Zhang, S.-C. Quantum anomalous hall effect with higher plateaus. *Phys. Rev. Lett.* **111**, 136801 (2013).
19. Fang, C., Gilbert, M. J. & Bernevig, B. A. Large-Chern-number quantum anomalous hall effect in thin-film topological crystalline insulators. *Phys. Rev. Lett.* **112**, 046801 (2014).
20. Wilczek, F. & Shapere, A. *Geometric Phases in Physics* (World Scientific, 1989).
21. Kane, C. L. & Mele, E. J. Quantum spin Hall effect in graphene. *Phys. Rev. Lett.* **95**, 226801 (2005).
22. Chittari, B. L., Chen, G., Zhang, Y., Wang, F. & Jung, J. Gate-tunable topological flat bands in trilayer graphene boron-nitride Moiré superlattices. *Phys. Rev. Lett.* **122**, 016401 (2019).
23. Ge, J. et al. High-Chern-number and high-temperature quantum Hall effect without Landau levels. *Natl Sci. Rev.* **7**, 1280–1287 (2020).
24. Thouless, D. J., Kohmoto, M., Nightingale, M. P. & den Nijs, M. Quantized Hall conductance in a two-dimensional periodic potential. *Phys. Rev. Lett.* **49**, 405–408 (1982).
25. Haldane, F. D. M. Model for a quantum hall effect without Landau levels: condensed-matter realization of the 'parity anomaly'. *Phys. Rev. Lett.* **61**, 2015–2018 (1988).
26. Zhang, Y., Tan, Y.-W., Stormer, H. L. & Kim, P. Experimental observation of the quantum Hall effect and Berry's phase in graphene. *Nature* **438**, 201–204 (2005).
27. Tomita, A. & Chiao, R. Y. Observation of Berry's topological phase by use of an optical fiber. *Phys. Rev. Lett.* **57**, 937–940 (1986).
28. Leek, P. J. et al. Observation of Berry's phase in a solid-state qubit. *Science* **318**, 1889–1892 (2007).
29. Roushan, P. et al. Observation of topological transitions in interacting quantum circuits. *Nature* **515**, 241–244 (2014).
30. Schroer, M. D. et al. Measuring a topological transition in an artificial spin-1/2 system. *Phys. Rev. Lett.* **113**, 050402 (2014).
31. Abanin, D. A., Kitagawa, T., Bloch, I. & Demler, E. Interferometric approach to measuring band topology in 2D optical lattices. *Phys. Rev. Lett.* **110**, 165304 (2013).
32. Wang, L., Soluyanov, A. A. & Troyer, M. Proposal for direct measurement of topological invariants in optical lattices. *Phys. Rev. Lett.* **110**, 166802 (2013).
33. Lin, Y.-J., Compton, R. L., Jiménez-García, K., Porto, J. V. & Spielman, I. B. Synthetic magnetic fields for ultracold neutral atoms. *Nature* **462**, 628–632 (2009).
34. Jotzu, G. et al. Experimental realization of the topological Haldane model with ultracold fermions. *Nature* **515**, 237–240 (2014).
35. Doherty, M. W. et al. The nitrogen-vacancy colour centre in diamond. *Phys. Rep.* **528**, 1–45 (2013).
36. Zhang, K., Nusran, N. M., Slezak, B. R. & Gurudev Dutt, M. V. Experimental limits on the fidelity of adiabatic geometric phase gates in a single solid-state spin qubit. *New J. Phys.* **18**, 053029 (2016).
37. Boyers, E., Crowley, P. J. D., Chandran, A. & Sushkov, A. O. Exploring 2D synthetic quantum Hall physics with a quasiperiodically driven qubit. *Phys. Rev. Lett.* **125**, 160505 (2020).
38. Kong, F. et al. Direct measurement of topological numbers with spins in diamond. *Phys. Rev. Lett.* **117**, 060503 (2016).
39. Chen, M. et al. A synthetic monopole source of Kalb-Ramond field in diamond. *Science* **375**, 1017–1020 (2022).
40. Gritsev, V. & Polkovnikov, A. Dynamical quantum Hall effect in the parameter space. *Proc. Natl Acad. Sci.* **109**, 6457–6462 (2012).
41. Wilczek, F. & Zee, A. Appearance of gauge structure in simple dynamical systems. *Phys. Rev. Lett.* **52**, 2111–2114 (1984).
42. Qi, X.-L., Hughes, T. L. & Zhang, S.-C. Topological field theory of time-reversal invariant insulators. *Phys. Rev. B* **78**, 195424 (2008).
43. Smeltzer, B., Childress, L. & Gali, A. 13 C hyperfine interactions in the nitrogen-vacancy centre in diamond. *N. J. Phys.* **13**, 025021 (2011).

AUTHOR CONTRIBUTIONS

J.L. and K.A. contributed equally to this work. The project was conceived by J.L. and K.A., and supervised by R.L.W. J.L., K.A., and H.Z. designed the experimental set-up. J.L., K.A., and M.J.K. designed the measurement protocol. J.L. and K.A. performed the measurements and analysed the data. All authors contributed to the discussion and preparation of the manuscript.

COMPETING INTERESTS

The authors declare no competing interests.

ADDITIONAL INFORMATION

Supplementary information The online version contains supplementary material available at https://doi.org/10.1038/s41534-023-00732-6.

Correspondence and requests for materials should be addressed to Ronald L. Walsworth.

Reprints and permission information is available at http://www.nature.com/reprints

Publisher's note Springer Nature remains neutral with regard to jurisdictional claims in published maps and institutional affiliations.